optica

Far-field diffraction microscopy at λ/10 resolution: supplementary material

TING ZHANG[1], CHARANKUMAR GODAVARTHI[1], PATRICK C. CHAUMET[1], GUILLAUME MAIRE[1], HUGUES GIOVANNINI[1], ANNE TALNEAU[2], MARC ALLAIN[1], KAMAL BELKEBIR[1], AND ANNE SENTENAC[1]

[1]*Aix Marseille Université, CNRS, Centrale Marseille, Institut Fresnel, UMR 7249, 13013 Marseille, France*
[2]*CNRS, Lab. Photon & Nanostruct, 91460 Marcoussis, France*
[*]*Corresponding author: anne.sentenac@fresnel.fr*

Published 7 June 2016

This document provides supplementary information to "Far-field diffraction microscopy at lambda/10 resolution," http://dx.doi.org/10.1364/optica.3.000609. It describes the experimental set-up of the full-polarized tomographic diffraction microscope and provides details on the reconstruction algorithm that is able to take advantage of an approximate knowledge of the target permittivity. A noise analysis and a comparison of the reconstructions obtained from synthetic and experimental data illustrate the performances of the imaging tool.
http://dx.doi.org/10.1364/optica.3.000609.s001

The sample to be imaged is described everywhere by a known relative permittivity $\varepsilon_{\text{background}}$ except in a bounded domain Ω where it is equal to ε.The sample contrast is defined as $\chi = \varepsilon - \varepsilon_{\text{background}}$ which is null outside Ω and unknown in Ω. In our configuration, the background medium consists in two semi-infinite media, air and silicon, separated by a planar interface at $z = 0$. We assume that Ω is entirely included in air.

The aim of the Tomographic Diffraction Microscope (TDM) is to retrieve $\chi(\mathbf{r})$ in Ω from the measurements of the far-field $\mathbf{f}_{l,m}^{\text{mes}}$ scattered by the medium in the $\mathbf{k}_m$ directions, $m = 1, \cdots, M$, for L plane wave illuminations of wavevector $\mathbf{k}_l$, $l = 1, \cdots, L/2$, and two independent polarization states. For this matter, we have implemented a calibrated experiment that yields the sample scattered far-field for plane wave illuminations, we have used a rigorous model for simulating the far-field $\mathbf{f}_{l,m}^{rmsim}$ for a given estimate of χ and we have developed an efficient inversion method, based on this model, that takes advantage of *a priori* information on the permittivity values.

1. EXPERIMENTAL SETUP

The Tomographic Diffraction Microscopy setup is basically an interferometric reflection microscope and is fully described in [1]. It permits to detect the amplitude, phase and polarization of the field scattered by the sample for various illuminations S1. The light source is a super continuum laser (NKT Photonics SuperK Extreme EXW-12), which is filtered at 475 nm with a spectral width of 6 nm thanks to a variable bandpass filter (NKT Photonics SuperK Varia). It is then linearly polarized and divided into two parts. The first one is the illumination path: the laser is directed towards a rotating mirror M (Newport FSM-300) which is optically conjugated with the object plane in front of the objective OL (Zeiss Epiplan-Apochromat 50$\times$ with numerical aperture NA$=$ 0.95 in air). Changing the orientation of the mirror permits to illuminate the same zone of the sample with various illumination angles. The collimated beam illuminates the sample through the objective, part of it is reflected by the sample, collected by the objective and detected on a sCMOS camera (Andor Zyla) optically conjugated with the object plane, with a global magnification of about 300. The second light path is the reference path: the beam is spatially filtered with a pinhole P and collimated to obtain an aberration free reference wave. This beam is superimposed thanks to beam splitter BS_3 to the reflected field imaged on the camera. Off-axis digital holography then permits to retrieve single shot wise the amplitude and phase of the field, projected onto the polarization of the reference field, at the image plane. To retrieve all the components of the field for two incident polarization, two half-wave plates have been placed in the illumination and detection paths, respectively (HW_1 and HW_2). They are used to generate two polarization bases for both the reference and incident field. Hence, for each incident angle, four measurements are performed.

To form the scattered far-field, two-dimensional Fourier transforms are applied to the four complex image fields. The value of the specular reflected beam, which is assumed to be negligibly perturbed by the sample, is used to calibrate the phase and amplitude of each Fourier hologram. Then,

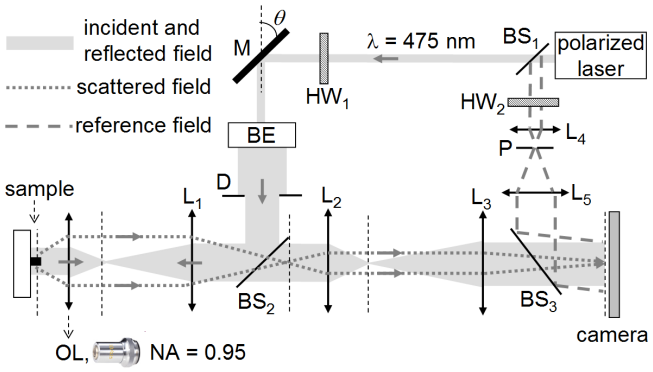

Fig. S1. Sketch of the experimental set-up: M, rotating mirror; BE, beam expander; D, diaphragm; OL, objective lens; L_1, tube lens; $L_{2,3}$, relay lenses ($f' = 3.5$ cm and 20 cm, respectively); $BS_{1,\cdots,3}$, beam splitters; P, pinhole; $HW_{1,2}$, half wave plates.

the four holograms are combined so as to form the vectorial transverse scattered far-fields along the directions allowed by the microscope objective for both TE and TM polarization states of the illumination, namely $\mathbf{f}_{l,m}^{\text{mes}}$ [1].

2. FORMULATION OF THE FORWARD SCATTERING PROBLEM

The simulation of the field scattered by a given sample contrast χ is performed thanks to the dipole discrete approximation (DDA) [2, 3]. This well known method is briefly described herein to introduce the notations used for the inverse problem.

The objects under study are represented by a cubic array of N polarizable subunits and the field at each subunit is expressed with the following self-consistent equation

$$\mathbf{E}(\mathbf{r}_i) = \mathbf{E}^{\text{inc}}(\mathbf{r}_i) + \sum_{j=1}^{N} \mathbf{G}(\mathbf{r}_i, \mathbf{r}_j)\chi(\mathbf{r}_j)\mathbf{E}(\mathbf{r}_j), \qquad \textbf{(S1)}$$

where $\mathbf{E}^{\text{inc}}(\mathbf{r}_i)$ denotes the incident field at the position $\mathbf{r}_i$, $\chi(\mathbf{r}_j) = \varepsilon(\mathbf{r}_j) - \varepsilon_{\text{background}}$ is the permittivity contrast and $\mathbf{G}$ is the Green function that accounts for the substrate. In other terms, $\mathbf{G}(\mathbf{r}_i, \mathbf{r}_j)\mathbf{p}$ represents the field at $\mathbf{r}_i$ radiated by a dipole $\mathbf{p}$ placed at $\mathbf{r}_j$ in the background medium.

Once the linear system represented by Eq. (S1) is solved, the scattered far-field in the $\mathbf{k}$ direction, $\mathbf{f}(\mathbf{k})$, can be computed with

$$\mathbf{f}(\mathbf{k}) = \sum_{j=1}^{N} \mathbf{G}^{\text{d}}(\mathbf{k}, \mathbf{r}_j)\chi(\mathbf{r}_j)\mathbf{E}(\mathbf{r}_j), \qquad \textbf{(S2)}$$

where $\mathbf{G}^{\text{d}}$ is the Green function that accounts for the substrate in far field [4, 5].

The self consistent equation, Eq. (S1), can be rewritten in a more condensed form as

$$\mathbf{E} = \mathbf{E}^{\text{inc}} + \mathbf{A}\chi\mathbf{E}, \qquad \textbf{(S3)}$$

where $\mathbf{A}$ is a square matrix of size $(3N \times 3N)$ and contains all the Green function $\mathbf{G}(\mathbf{r}_i, \mathbf{r}_j)$. $\mathbf{E}$ and $\mathbf{E}^{\text{inc}}$ are the total field and the incident field, respectively.

In a TDM experiment, the scattered field is collected along M observation directions for L successive illuminations. Let $\mathbf{f}_l$ be the column vector of dimension $3M$ (the 3 stands for the three components along (x, y, z) of the field) corresponding to the scattered fields $\mathbf{f}_{l,m}$, $m = 1, \cdots, M$ obtained for the l-th illumination. We can rewrite the far field equation, Eq. (S2), in the following condensed form

$$\mathbf{f}_l = \mathbf{B}\chi\mathbf{E}_l, \qquad \textbf{(S4)}$$

where $l = 1, \cdots, L$, and $\mathbf{B}$ is a matrix of size $(3M \times 3N)$. The matrix $\mathbf{B}$ contains the Green function $\mathbf{G}^{\text{d}}(\mathbf{k}_m, \mathbf{r}_j)$, where $\mathbf{r}_j$ denotes a point in the discretized object, $j = 1, \cdots, N$, while $\mathbf{k}_m$ is an observation direction, $m = 1, \cdots, M$. Note that $\mathbf{B}$ does not depend on the angle of incidence.

3. ANALYZING THE NOISE ON THE SCATTERED FAR-FIELDS AND REDUCING ITS INFLUENCE

In this section, we consider the two star-samples depicted in Figs. (2,3) of the letter and we compare the experimental scattered far-field to the theoretical one. The latter is simulated using the Coupled Dipole Method with the contrast distribution χ_{true} suggested by the electronic microscope image. Figures S2 and S4 show the modulus of the three components of the far-field for the 'large' and 'small' star, respectively. These figures point out calibration errors and additive noise. The calibration error is about 2 for incidences close to the edge of the numerical aperture and decreases to 1 for incidences close to the normal incidence. The additive noise is present for all incidences and can be interpreted as speckle field stemming from dust outside the sample. As expected, it is more disturbing for the small star-sample than for the 'large' one, compare Fig. S4 with Fig. S2. This observation is confirmed by the comparison of the experimental and theoretical diffracted field phases in Figs. S3 and S5.

In order to diminish the influence of the speckle noise in the inversion, we have implemented an efficient pre-processing of the data prior the inversion. This processing is based on DORT (french acronym for Décomposition de l'Opérateur de Retournement Temporel) method which is the monochromatic counterpart of the time reversal method. It has been successfully applied to the retrieval of scatterers present in a highly cluttered medium for the two-dimensional problem in Ref. [6] and in Refs. [7, 8] for the three-dimensional case. The DORT procedure requires to record the field (amplitude and phase) scattered by the sample for various illuminations in order to build the scattering matrix $\mathbf{F}$ of the scatterer, *i.e.* a matrix that relies the incoming field to the outgoing one. In our case, $\mathbf{F} = \{\mathbf{f}_{l,m}^{\text{mes}}\}$ and it relies the illumination space to the observation space. It has been shown that singular eigenvectors of $\mathbf{F}$ in the illumination space correspond to incident beams that focus specifically on the target [8]. By limiting the incident intensity to a small region about the sample, these focusing illuminations lower significantly the speckle noise.

Hereafter, we replace the L plane wave illumination by the L singular eigenvectors of the scattering matrix $\mathbf{F}$. Thus, the input data in the inversion scheme are now given by the L scattered far-field associated to these L focusing illuminations. Using these synthesized fields instead of the standard ones turns out to significantly improve the reconstructions whenever the targets under test are present in a noisy environment and/or the measurements are corrupted with a high level of noise. From now on, we refer as scattered and incident fields the fields constructed thanks to the singular value decomposition of the scattering matrix $\mathbf{F}$.

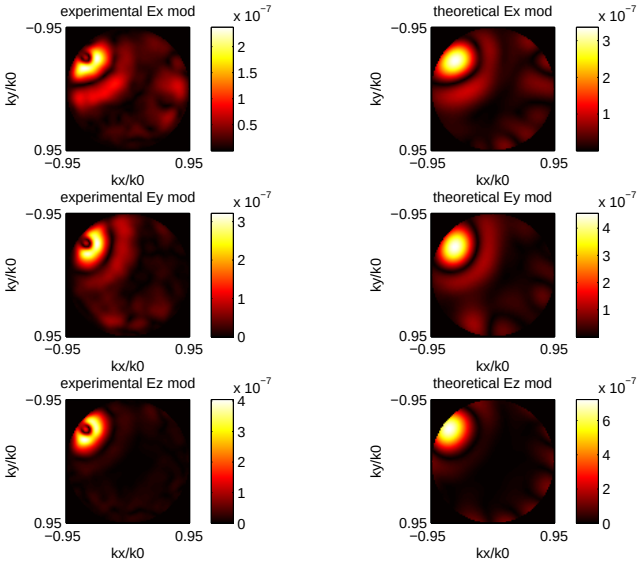

Fig. S2. Modulus of the diffracted field experimentally and theoretically for the star with width about 97 nm.

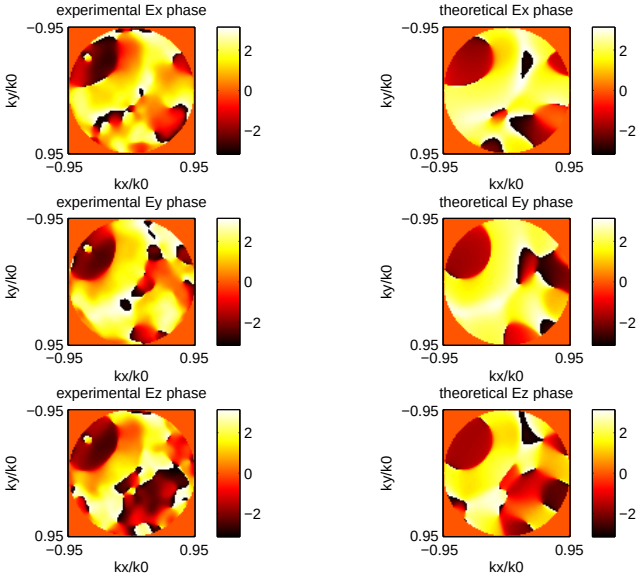

Fig. S3. Phase of the diffracted field experimentally and theoretically for the star with width about 97 nm.

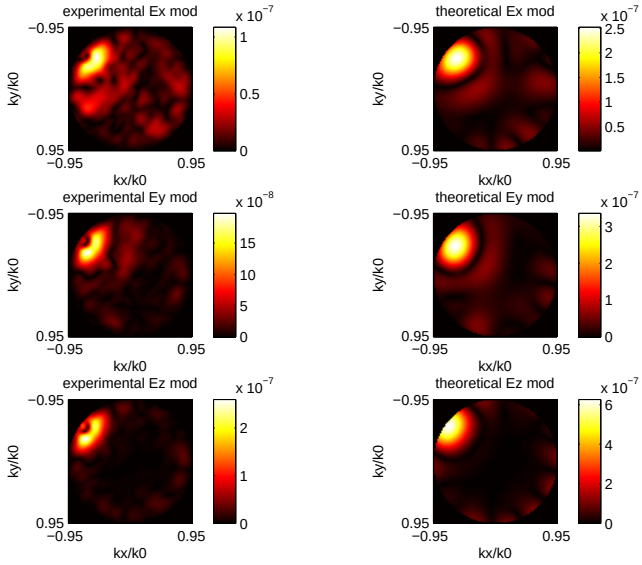

Fig. S4. Modulus of the diffracted field experimentally and theoretically for the star with width about 76 nm.

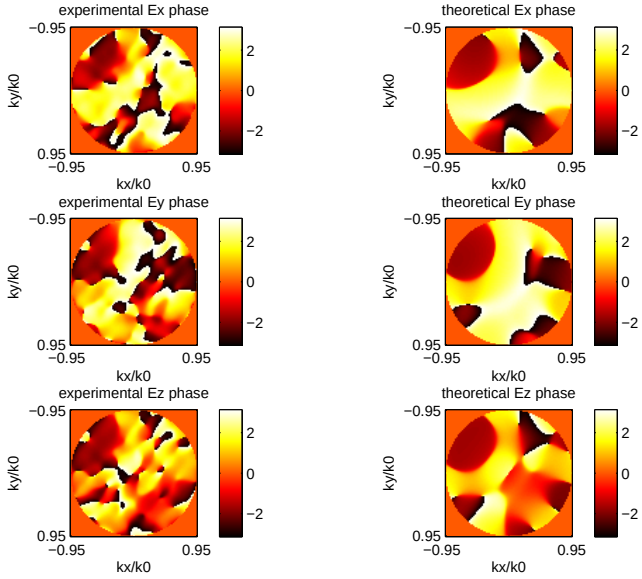

Fig. S5. Phase of the diffracted field experimentally and theoretically for the star with width about 76 nm.

4. INVERSION ALGORITHM

The realm of inverse scattering problem is to determine the relative permittivity distribution of samples from the measured scattered far-field. The most popular strategies to solve these nonlinear and ill-posed problem is to determine the parameters of interest iteratively. In the present paper, two iterative schemes have been applied. The first one is the hybrid-iterative method that does not require the knowledge of the constitutive material of samples under test. This technique has been already presented by the authors elsewhere and therefore will not be described here, for details see Refs. [9, 10].

In this section, we focus on the second technique which accounts for a partial knowledge of the sample permittivity and is referred as the Bounded Inverse Method (BIM). The objective is to estimate χ in the investigating domain Ω. The basic ideas underlying BIM is to build up iteratively a sequence of χ_n by minimizing a cost functional of the form [11, 12]

$$\mathcal{F}(\chi_n) = W_\Gamma \sum_{l=1}^{L} \|\mathbf{f}_l^{\text{mes}} - \mathbf{f}_l^{\text{sim}}\|^2 = W_\Gamma \sum_{l=1}^{L} \|\mathbf{f}_l^{\text{mes}} - \mathbf{B}\chi_n \mathbf{E}_{l,n}\|^2, \quad \textbf{(S5)}$$

with $W_\Gamma = \left(\sum_{l=1}^{L} \|\mathbf{f}_l^{mes}\|^2\right)^{-1}$ and where $\mathbf{f}_l^{mes}$ is the experimental data and $\mathbf{E}_l^{sim}$ is the simulated field scattered by the best available estimated sample contrast χ_n.

We now assume that the relative permittivity distribution in Ω varies within the interval $[\varepsilon_{\text{background}}, \varepsilon_{\text{ref}}]$ where ε_{ref} is the known permittivity of the target. To enforce a binary behavior to the permittivity distribution, the contrast χ is rewritten in the form,

$$\chi(\xi) = (\varepsilon_{\text{ref}} - \varepsilon_{\text{background}}) \left[1 - \exp(-\xi^2)\right], \quad \textbf{(S6)}$$

where ξ is an auxiliary function which is the new parameter that is minimized in the inversion algorithm. The derivative of χ with respect to ξ reads as:

$$\frac{d\chi}{\mathrm{d}\xi} = (\varepsilon_{\text{ref}} - \varepsilon_{\text{background}}) \left[2\xi \exp(-\xi^2)\right]. \quad \textbf{(S7)}$$

In Fig. S6 we plot χ and $\chi' = \frac{d\chi}{\mathrm{d}\xi}$ versus ξ. Using this formulation, small values of ξ correspond to the background medium ($\chi = 0$) and large values of ξ correspond to the target, $\varepsilon_{\text{ref}} - \varepsilon_{\text{background}}$.

The inverse problem is then reformulated as building a sequence of ξ_n so as to minimize the cost functional $\mathcal{G}(\xi_n) = \mathcal{F}[\chi(\xi_n)]$. A sequence of auxiliary function ξ_n is then retrieved according to the updating relation $\xi_n = \xi_{n-1} + \alpha_n^\xi d_n^\xi$, where d_n^ξ is an updating direction and α^ξ is a real valued scalar that minimizes the cost function $F(\alpha_n^\xi) = \mathcal{F}[\chi(\xi_{n-1} + \alpha_n^\xi d_n^\xi)]$.

Unfortunately, due to the transformation introduced in Eq. (S6), there is no analytic expression of α^ξ that minimizes the cost function F. Now, the numerical determination of this minimum [13] is severely time consuming. We have thus proposed an alternative approach which consists in assuming that $\alpha_n^\xi d_n^\xi$ is small enough so that the permittivity contrast χ_n can be expanded to first order in ξ_{n-1}. The exponential term in Eq. (S6) is then expressed as $\exp(-\xi_n^2) = \exp(-\xi_{n-1}^2) - 2\xi_{n-1}\alpha_n^\xi d_n^\xi \exp(-\xi_{n-1}^2)$, and subsequently

$$\begin{aligned} \chi_n &\approx \chi_{n-1} + 2\alpha_n^\xi (\varepsilon_{\text{ref}} - \varepsilon_{\text{background}}) \xi_{n-1} d_n^\xi \exp(-\xi_{n-1}^2), & \textbf{(S8)} \\ &\approx \chi_{n-1} + \alpha_n^\xi v_n, & \textbf{(S9)} \end{aligned}$$

with,

$$v_n = 2(\varepsilon_{\text{ref}} - \varepsilon_{\text{background}}) \xi_{n-1} d_n^\xi \exp(-\xi_{n-1}^2). \quad \textbf{(S10)}$$

Substituting this expression of χ_n into the cost function F, leads to a polynomial expression with respect to the scalar coefficient α_n^ξ,

$$\begin{aligned} \mathcal{F}_n(\chi_n) &= W_\Gamma \sum_{l=1}^{L} \Big(\|\mathbf{h}_{l,n-1}\|^2 + (\alpha_n^\xi)^2 \|\mathbf{B}v_n \mathbf{E}_{l,n}\|^2 \\ &- 2\alpha_n^\xi \mathrm{Re}\left\langle \mathbf{h}_{l,n-1} | \mathbf{B}v_n \mathbf{E}_{l,n} \right\rangle \Big). \quad \textbf{(S11)} \end{aligned}$$

Writing down the necessary condition of F to be minimum, *i. e.* $\frac{\partial \mathcal{F}_n(\chi_n)}{\partial \alpha_n^\xi} = 0$, provides the unique minimum of $\mathcal{F}_n(\chi_n)$

$$\alpha_n^\xi = W_\Gamma \sum_{l=1}^{L} \frac{\mathrm{Re}\left\langle \mathbf{h}_{l,n-1} | \mathbf{B}v_n \mathbf{E}_{l,n} \right\rangle}{\|\mathbf{B}v_n \mathbf{E}_{l,n}\|^2}. \quad \textbf{(S12)}$$

This analytic expression of α_n^ξ reduces drastically the time computation.

As the updating direction d_n^ξ, the authors took the standard Polak-Ribière conjugate-gradient directions [14].

$$d_n^\xi = g_n^\xi + \gamma_n^\xi d_{n-1}^\xi, \quad \gamma_n^\xi = \frac{\left\langle g_n^\xi, g_n^\xi - g_{n-1}^\xi \right\rangle_\Omega}{\|g_{n-1}^\xi\|_\Omega^2}, \quad \textbf{(S13)}$$

where g_n^ξ is the gradient of the cost functional $\mathcal{G}(\xi)$ with respect to the parameter ξ assuming that the internal fields do not change [13]:

$$\begin{aligned} g_n^\xi &= g_n^\chi \frac{\mathrm{d}\chi}{\mathrm{d}\xi}, & \textbf{(S14)} \\ g_n^\chi &= -W_\Gamma \sum_{l=1}^{L} \mathbf{E}_{l,n-1}^* . \mathbf{B}^\dagger \mathbf{h}_{l,n-1}. & \textbf{(S15)} \end{aligned}$$

By construction, the updating direction associated to $\chi' = \frac{\mathrm{d}\chi}{\mathrm{d}\xi}$ tends towards 0 for small and large values of ξ. Hence, the transformation introduced in Eq. (S7) promotes the extreme values $\varepsilon_{\text{background}}$ and ε_{ref} for the estimated permittivity.

In all reported reconstructions the initial guess is a weak scattering object with constant contrast $\chi^{\text{initial}} = 0.01$ which yields approximately the same level of scattered far-field amplitude and the pixel size is 20 nm. The convergence of the conjugate gradient technique proved relatively slow with oscillating values of the cost function. To speed up the algorithm we thus implemented a fast iterative shrinkage-thresholding (FISTA) algorithm [15] using only the simple gradient direction *i. e.* $d_n^\xi = g_n^\xi$. With FISTA only 50 iterations were needed to get the convergence. The reconstruction of the stars took approximately 3 hours on a computer with processor Intel(R) Xeon(R) at 3.40 GHz.

5. THREE-DIMENSIONAL INVERSION OF THE STAR-SAMPLES, SYNTHETIC AND EXPERIMENTAL DATA

In this section, we compare the reconstructions of the star-samples when the inversion is performed on (quasi noiseless) synthetic data and on experimental data. In the first case, the stars are retrieved almost perfectly, see Fig. S7 with a resolution corresponding to the size of the pixel, 20 nm. The comparison between Fig. S7 and the images obtained from the experimental

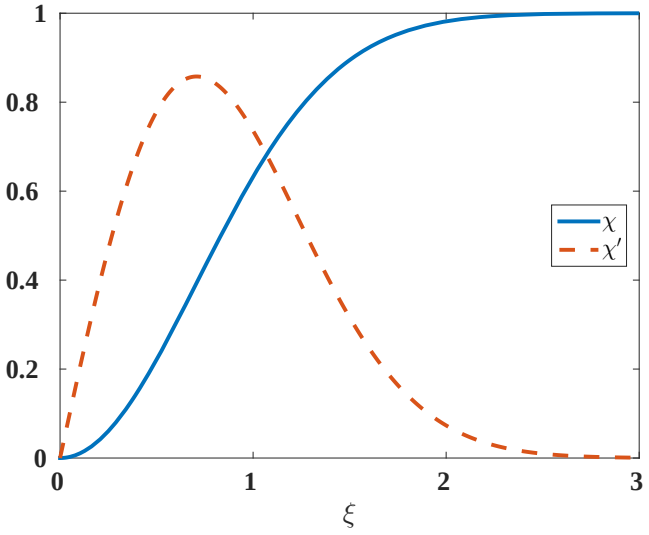

Fig. S6. Expression of the contrast χ and its derivative $\chi' = \frac{d\chi}{d\xi}$ versus ξ.

data, see Figs. (2,3) of the letter, allows one to visualize the non-negligible influence of noise on the reconstructions.

Figure S8 reports the three-dimensional iso-contour (taken at the value $\varepsilon = 1.9$ in order to get the air-resin interface) of the reconstructed star-samples obtained from synthetic data and experimental data. It is observed that the speckle noise and the calibration errors yields an overestimation of the sample height at the apex of the branches of the star.

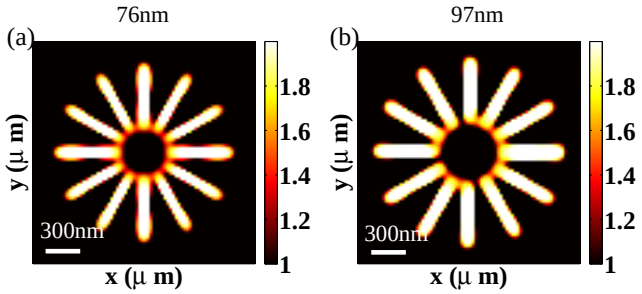

Fig. S7. Reconstruction of the star-samples from synthetic data (a) Star with 76 nm width. (b) Star with 97 nm width.

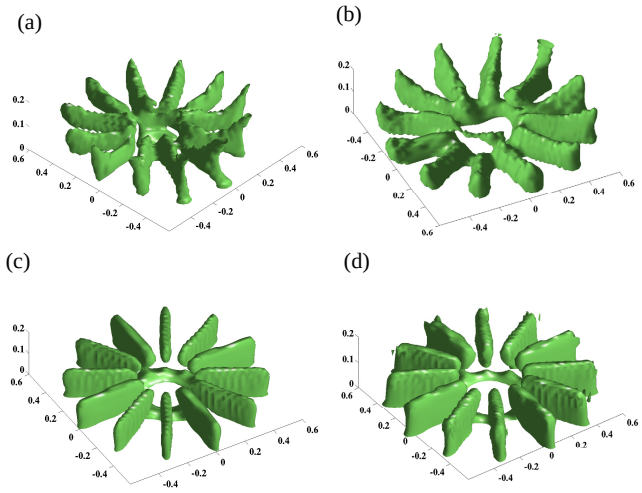

Fig. S8. Three dimensional iso-contour of the permittivity distribution of the star-samples obtained from synthetic (c,d) and experimental data (a,b). The iso surface is taken at $\varepsilon = 1.9$ in order to get the air-resin interface. (a) star width 76 nm width, (b)star width 97 nm (c) star width 76 nm width, (d) star width 97 nm width.

REFERENCES

1. C. Godavarthi, T. Zhang, G. Maire, P. C. Chaumet, H. Giovannini, A. Talneau, K. Belkebir, and A. Sentenac, "Superresolution with full-polarized tomographic diffractive microscopy," J. Opt. Soc. Am. A **32**, 287–292 (2015).
2. E. M. Purcell and C. R. Pennypacker, "Scattering and absorption of light by nonspherical dielectric grains," Astrophys. J. **186**, 705–714 (1973).
3. P. C. Chaumet, A. Sentenac, and A. Rahmani, "Coupled dipole method for scatterers with large permittivity," Phys. Rev. E **70**, 036606–6 (2004).
4. P. C. Chaumet, K. Belkebir, and A. Sentenac, "Superresolution of three-dimensional optical imaging by use of evanescent waves," Opt. Lett. **29**, 2740–2742 (2004).
5. K. Belkebir, P. C. Chaumet, and A. Sentenac, "Superresolution in total internal reflection tomography," J. Opt. Soc. Am. A **22**, 1889–1897 (2005).
6. A. Dubois, K. Belkebir, and M. Saillard, "Localization and characterization of two-dimensional targets buried in a cluttered environment," Inverse Probl. **20**, S63–S79 (2004).
7. T. Zhang, P. C. Chaumet, A. Sentenac, and K. Belkebir, "Three-dimensional imaging of targets buried in a cluttered semi-infin ite medium," J. Appl. Phys. **114**, 143101 (2013).
8. T. Zhang, C. Godavarthi, P. C. Chaumet, G. Maire, H. G. nnini, A. Talneau, C. Prada, A. Sentenac, and K. Belkebir, "Tomographic diffractive microscopy with agile illuminations for imaging targets in a noisy background," Opt. Lett. **40**, 573–576 (2015).
9. E. Mudry, P. C. Chaumet, K. Belkebir, and A. Sentenac, "Electromagnetic wave imaging of three-dimensional targets using a hybrid iterative inversion method," Inverse Probl. **28**, 065007 (2012).
10. T. Zhang, P. C. Chaumet, E. Mudry, A. Sentenac, and K. Belkebir, "Electromagnetic wave imaging of targets buried in a cluttered medium u sing a hybrid inversion-dort method," Inverse Probl. **28**, 125008 (2012).
11. K. Belkebir, P. C. Chaumet, and A. Sentenac, "Influence of multiple scattering on three-dimensional imaging with optical diffraction tomography," J. Opt. Soc. Am. A **23**, 586–595 (2006).
12. K. Belkebir and M. Saillard, "Special section on testing inversion algorithms against experimental data: inhomogeneous targets," Inverse Probl. **21**, S1–S3 (2005).
13. P. C. Chaumet, K. Belkebir, and A. Sentenac, "Experimental microwave imaging of three-dimensional targets with different inversion procedures," J. Appl. Phys. **106**, 034901–8 (2009).

14. W. H. Press, B. P. Flannery, S. A. Teukolski, and W. T. Vetterling, *Numerical recipes. The art of scientific computing* (Cambridge University Press, 1986).
15. A. Beck and M. Teboulle, "A fast iterative shrinkage-thresholding algorithm for linear inverse problems," SIAM Journal on Imaging Sciences **2**, 183–202 (2009).